

STRENGTH AND PLASTICITY

Structure, Phase Composition, and Mechanical Properties of a High Strength Steel with Transition Carbide η -Fe₂C

Yu. I. Borisova^{a, b, *}, R. V. Mishnev^{a, b}, E. S. Tkachev^{a, b}, T. V. Kniaziuk^{b, c},
S. M. Gaidar^a, and R. O. Kaibyshev^a

^a Russian State Agrarian University—Moscow Timiryazev Agricultural Academy, Moscow, 127434 Russia

^b Belgorod State National Research University, Belgorod, 308015 Russia

^c Central Research Institute of Structural Materials Prometei, National Research Center Kurchatov Institute,
St. Petersburg, 191015 Russia

*e-mail: borisova_yu@bsu.edu.ru

Received May 7, 2023; revised August 19, 2023; accepted August 25, 2023

Abstract—The effects of quenching and tempering on the structure, phase composition, and mechanical properties of the Fe–0.34C high strength steel with 1.77 wt % Si are studied. The tempering at temperatures up to 500°C barely has an effect on the structural characteristics of packet martensite formed during quenching. The precipitation of intermediate (transition) η -carbide particles at tempering temperatures in the range of 200–400°C leads to increases in the yield strength to 1490 MPa and in the impact toughness to 35 J/cm². The determined temperature of the ductile–brittle transition of the steel tempered at 200°C is about –50°C. A decrease in the impact toughness and a decrease in the proportion of ductile fracture with a decrease in the test temperature are accompanied by a transition from transgranular to intergranular fracture. The precipitation of cementite particles along the boundaries of the laths and blocks is observed after tempering at 500°C. This leads to a decrease in the yield strength, while the impact toughness of the steel remains unchanged.

Keywords: high strength steel, tempering, microstructure, carbide, mechanical properties, impact toughness, ductile–brittle transition

DOI: 10.1134/S0031918X23602445

INTRODUCTION

Currently, manufacturers of agricultural and earth-moving equipment are in demand for high-strength steels with a yield strength of above 1400 MPa, from which materials it is planned to manufacture working components of earth-moving machines. These kinds of steels are subject to requirements for a combination of high hardness, strength, wear resistance, good ductility, and satisfactory impact toughness [1–5]. High-strength steels are used in aircraft manufacturing, rocketry, and space technology [4, 5]. Their use in the production of cars, transport and earth-moving equipment is hampered by their high cost [1, 2]. Among all types of high-strength steels, only low alloyed steels with transition carbides of the ϵ/η -Fe₂C type are suitable for use in civil engineering industries because of cost restrictions [4]. This class of steels includes medium carbon steel 300M, which is an improved version of steel AISI4340 with a high Si content (1.6 wt %) (Table 1) [4–6]. This steel shows high yield strength, good ductility, and satisfactory impact toughness after quenching and tempering (Q&T) at 300°C (Table 1) [7]. To obtain this set of properties, steel 300M is subjected to vacuum arc remelting (VAR). To produce

high strength steels for the use in agricultural machinery and vehicles, it is advisable to replace VAR with electroslag remelting (ESR), which decreases the sulfur content and increases the toughness of steels with transition carbides [4, 7].

The unique combination of strength, ductility, and toughness in steel 300M is associated with the effect of Si on the processes that accompany Q&T [8–12]. In the quenching process, steel 300M retains up to 10% of austenite, which is saturated with carbon up to 1.5 wt % after low temperature tempering due to the redistribution of carbon from martensite [12–15]. As is known [2, 8–11, 15, 16], the addition of more than 1.5 wt % of Si to low alloyed steel suppresses the formation of cementite up to temperatures around 470°C, which ensures the presence of only transition carbides in the structure of steel tempered at temperatures of $\leq 400^\circ\text{C}$. The decomposition of retained austenite during low temperature tempering leads to the formation of transition carbides in bainitic ferrite [9, 17]. That is, phase transformations in low alloyed steels with a Si concentration of ≥ 1.5 wt % during tempering differ from transformations in steels with lower contents of Si [6, 9, 16–18]. Suppressing the formation of lamellar

Table 1. Chemical composition and mechanical properties of steels 300M and AISI4340 and the ductile–brittle transition temperature (DBTT) [3, 6] after quenching and low-temperature tempering (240–310°C)

Steel	300M	AISI4340
Chemical composition, wt %	Fe–(0.4–0.45)C–(1.45–1.80)Si–(0.7–0.95)Cr–(1.65–2.0)Ni–(0.3–0.5)Mo–(0.05–0.1)V–0.01P–0.01S	Fe–(0.37–0.43)C–(0.15–0.3)Si–(0.7–0.9)Cr–(1.65–2.0)Ni–(0.2–0.3)Mo–(0.6–0.8)Mn–0.04P–0.04S
Yield strength, MPa	1590	1407
Ultimate tensile strength, MPa	1923	1873
Total elongation, %	10	6
Impact toughness, J/cm ²	20	18
DBTT, °C	–17	–

Table 2. Chemical composition of the Fe–0.34 wt % C steel under study (Fe is base)

Elements	C	Si	Mn	Cr	Mo	Nb	Ti	B	Al	Σ(S + P)
Fe–0.34 C	0.34	1.77	1.35	0.56	0.20	0.04	0.031	0.002	≤ 0.01	≤ 0.012

cementite along the boundaries of packet martensite structures eliminates or weakens reversible temper brittleness [8, 9]. The microalloying with Nb and Ti is aimed both at the formation of two types of MX carbonitrides in the high temperature region to prevent recrystallization processes in austenite during hot deformation and at obtaining additional dispersion strengthening [19]. Russian steels of a similar class, which are developed on the basis of steel 30KhGSA, contain a higher Cr content and about 1 wt % Si [19]. They do not belong to the class of high strength steels, since their yield strength is ≤1300 MPa [20].

In this study, we investigated the effects of quenching and subsequent tempering (Q&T) on the structure and mechanical properties of high strength steel Fe–0.34C, which is characterized by the absence of Ni, an increased Mn content, a reduced carbon content, the presence of Nb, and the use of ESR to remove impurities instead of VAR in comparison with steel 300M (Table 2).

Scanning and TEM techniques were used to determine the effect of increased silicon content on the phase transitions occurring in the course of low temperature tempering in low alloyed medium carbon steels and to establish the relationship between the structure formed during low temperature tempering and the mechanical properties. Based on the obtained results, the possibility of using the Fe–0.34C steel as a high strength steel obtained with cost effective alloying and by simplified metallurgical technology was assessed [4, 5].

MATERIALS AND METHODS

The chemical composition of the studied Fe–0.34C steel obtained by the ESR method is given in Table 2. The ingot was homogenized at 1150°C for 4 h

with subsequent forging in the temperature range of 1150 to 950°C into the billet with dimensional sizes of 60 × 150 × 450 mm, which then cooled to room temperature in air. Thermal treatment of the samples included austenitization at a temperature of 900°C for 5 min, quenching in hot water, and subsequent tempering at temperatures of 200, 280, 400, and 500°C for 1 h with final cooling in air.

Equilibrium volume fractions of the phases were calculated in the Thermo-Calc software package using the TCFE7 thermodynamic base.

The differential scanning calorimetry (DSC) studies were performed on an SDT Q600 calorimeter (TA Instruments New Castle, DE, United States). The weight of the samples was about 142 mg; a protective atmosphere of pure argon was used. The samples were quenched in hot water from an austenitization temperature of 900°C and then heated with a rate of 10°C/min in a calorimeter. The dilatometry studies were performed using a DIL 805 hardening dilatometer from the same company. The dilatometric curve was obtained by cooling from a temperature of 900°C to a temperature of 330°C with a cooling rate of 200°C/s and then from 330°C to room temperature with a cooling rate of 53°C/s. Cylindrical samples with a length of 10 mm and a diameter of 3 mm were used in dilatometric studies.

Microstructures were studied by scanning electron microscopy (SEM) on a Quanta 600FEG microscope (FEI, Hillsboro, Oregon, United States) equipped with an analyzer of electron backscatter diffraction (EBSD) patterns and a system for misorientation mapping (OIM) and by transmission electron microscopy (TEM) on a Jeol JEM-2100 microscope (JEOL Ltd., Tokyo, Japan) with an INCA attachment for energy dispersive X-ray (EDX) analysis (Oxford Instruments, Oxfordshire, UK). Samples for SEM

and thin foils for TEM were prepared by electrolytic polishing and double sided jet electrochemical polishing with use of a 10% HClO_4 solution and a 90% CH_3COOH solution. To analyze phases, carbon replicas for subsequent investigation by TEM were obtained from the samples. Phases were identified by comparing the chemical composition data determined by the EDX method and from the electron diffraction patterns (TEM). Two EBSD maps were analyzed in each state. The resulting EBSD maps had an area of $100 \times 100 \mu\text{m}^2$ with a scanning step of $0.1 \mu\text{m}$. The average value of the coefficient characterizing the reliability of indexing the Kikuchi lines (Confidence Index, CI) of the EBSD patterns was in the range from 0.29 to 0.41. For EBSD patterns with a CI coefficient of more than 0.1, the fraction of correctly indexed Kikuchi lines is 95%, which indicates the high reliability of the obtained results [21]. For correct interpretation of EBSD patterns, points with a CI coefficient of less than 0.1 were excluded. The boundaries of the initial austenite grains and martensite packets were identified using algorithms for reconstructing the initial austenite structure with use of the MTEX toolkit implemented in the MATLAB program [10, 22]. The dislocation density was calculated by determining the average misorientation between adjacent points inside individual grains by means of Kernel function for EBSD maps [10, 23]:

$$\rho = \frac{2\theta}{bh}, \quad (1)$$

where θ is the average misorientation between adjacent points, $b = 0.25 \text{ nm}$ is the Burgers vector abs. value for $\alpha\text{-Fe}$, and h is the scanning step.

The volume fraction of retained austenite was determined by two methods. First, by calculating the quantitative ratio of points with fcc and bcc lattices identified on the surface of samples when analyzing EBSD patterns. Secondly, by determining the magnetic saturation of the sample using a Fischer Feritcope FMP30 ferritometer (Helmut Fischer GmbH, Sindelfingen, Germany). The error of the results obtained by different research methods did not exceed 0.2%.

Static tensile tests on flat samples with a calculated length of 35 mm and a cross section size of $7 \times 3 \text{ mm}$ were carried out on an Instron 5882 testing machine (Illinois ToolWorks Inc., Norwood, MA, United States) at room temperature. Dynamic impact tests in accordance with the ASTM E-23 standard were performed on Charpy specimens 55 mm in length and $10 \times 10 \text{ mm}$ in cross section with a 2 mm deep V-type concentrator with use of an Instron SI-1M impact driver (Instron corporation, Grove City, PA, United States) equipped with an Instron Dynatup Impulse system for recording diagrams. Two standard samples were tested in each determination of tensile and

impact toughness values. The spread in the obtained values of mechanical characteristics was no more than 10% for each state. The fracture surface of the tested Charpy samples was investigated using a Quanta 600 FEG scanning electron microscope. The remaining details of structural studies, DSC, dilatometry, and mechanical tests were described in previous studies [8–11, 24].

RESULTS AND DISCUSSION

Phase Transformations

According to thermodynamic calculations (Fig. 1a), the temperatures of the onset (A_{c1}) and completion (A_{c3}) of the austenitic transformation are 733 and 827°C , respectively. According to the analysis of the DSC curve (Fig. 1b), the corresponding temperatures were determined to be 761 and 886°C , respectively. One can see that the differences between the calculated and experimental temperatures of A_{c1} and A_{c3} are 28 and 50°C , respectively. Thus, the selected heating temperature for quenching ensures a completely austenitic structure.

According to thermodynamic calculations performed in the Thermo-Calc software package, the structure of the steel under study contains the following thermodynamically equilibrium carbides: M_3C , M_7C_3 , M_6C , and MC at temperatures below A_{c1} and M_{23}C_6 and MC at temperatures above A_{c3} . Vertical dotted lines indicate temperatures that correspond to the austenitization and tempering temperatures of the studied steel. It should be noted that the TCFE7 database does not contain transition carbides of the ϵ/η -carbide types, which can be precipitated during tempering at temperatures up to 420°C [4, 6, 8–11, 17, 18, 25–27], and can be used in calculations only for the phases shown in Fig. 1a. The maximum fractions of carbides M_{23}C_6 and M_6C were 0.07 and 0.32 vol %, respectively. The low volume fraction of M_6C carbides in the equilibrium phase composition at the temperature of the low temperature tempering process is explained by the small amount of Mo in the chemical composition of the steel. The volume fraction of M_3C cementite reaches 6 vol % at 550°C , which corresponds to the medium carbon steel with a ferrite–pearlite structure. In this case, the calculation of the equilibrium phase composition allows us to establish the following sequence of transitions: martensite $\rightarrow \text{M}_7\text{C}_3 \rightarrow \text{M}_3\text{C}$.

The data of dilatometric studies made it possible to determine the Martensite start (M_s) and martensite finish (M_f), which were found to be $M_s = 316^\circ\text{C}$ and $M_f \geq 140^\circ\text{C}$, respectively (Fig. 1c). Given that the difference between the end point of martensitic transformation (M_f) and the temperature of the quenching medium is about 100°C , it can be concluded that the

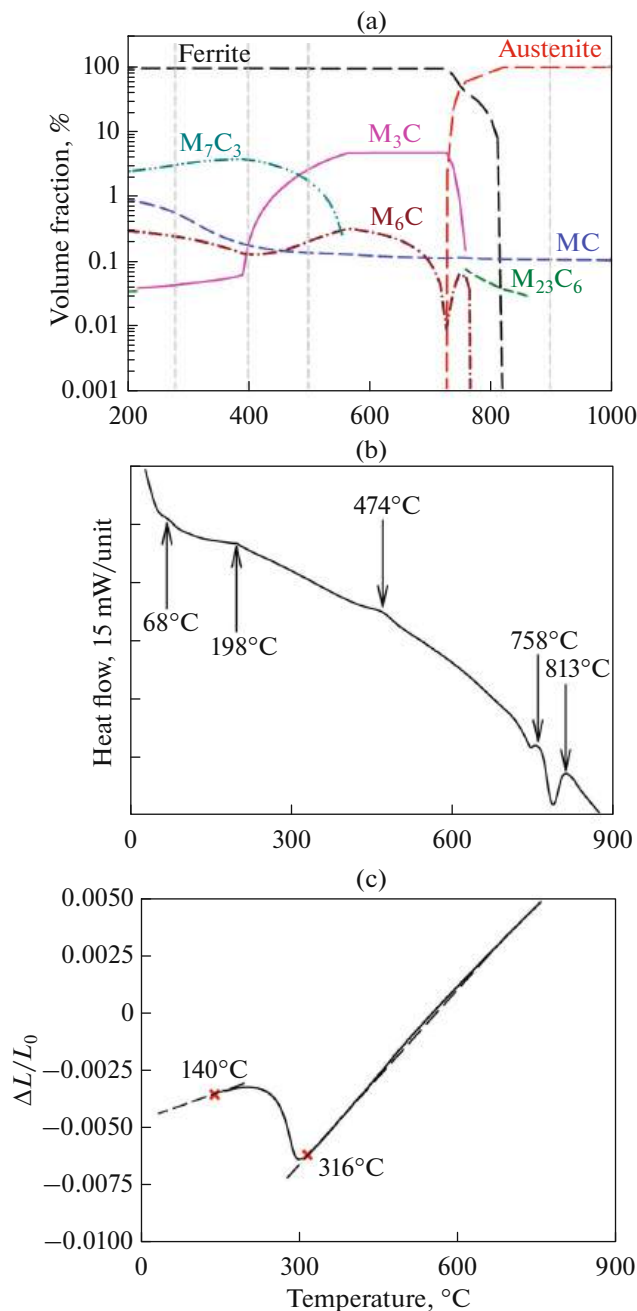


Fig. 1. (a) Temperature dependence of the equilibrium volume fraction of phases, (b) the heating mode DSC curve of the steel after quenching, and (c) the dilatometric curve obtained in the cooling mode.

applied treatment regime produces a martensitic structure with a small amount of retained austenite.

Figure 1b shows the results of a DSC analysis. A weak exothermic peak that is associated with the formation of carbon clusters [28] is observed at 68°C. The exothermic peak at 198°C may be associated with the onset of austenite decomposition. However, it is more likely that this peak is associated with the precip-

itation of transition carbides in view of the small amount of retained austenite (Table 3), the same as in other low alloyed steels undergone low temperature tempering [8–11]. The exothermic peak at 474°C is associated with the precipitation of cementite [8–11, 29]. Thus, the alloying with Si, Mo, and Cr increases the temperature of Fe_3C precipitation in the studied steel compared to steels with a low silicon content and a comparable carbon content [16, 18, 29]. It follows from the DSC data that partial decomposition of martensite is accompanied by the precipitation of transition carbides and the complete decomposition of martensite leads to the precipitation of cementite at temperatures close to 500°C. Accordingly, the steel structure will correspond to martensite with transition carbides after low temperature tempering and to ferrite with cementite after medium temperature tempering.

Microstructure

Misorientation maps and the fine structure of the studied steel after Q&T are shown in Figs. 2 and 3, and the structural characteristics are summarized in Table 3. The quenching process leads to the formation of a typical packet martensite structure that consists of packets, blocks, and laths, in which the boundaries of the prior austenite grains (PAGs) are inherited (Fig. 2) [8–11, 22, 30–32].

The mean size of PAGs is 23 μm (Table 3), and their shape is close to an equiaxed one (Fig. 2) characterized by small degrees of deformation during forging. Moreover, the ratio of the sizes of martensite packets to the sizes of PAGs is relatively small [8–10, 33] and equals $D_{\text{packet}} = 0.27 \times D_{\text{PAG}}$. This is due to the fact that packets with crystallographic orientation corresponding to no more than three different $\{111\}_\gamma$ planes are formed within an PAG (Figs. 2b and 2d) [30–32]. In PAGs with a size of more than 20 μm , six or more packets are observed (Figs. 2b and 2d). Among them, two and sometimes three packets are round in shape and consist of several blocks, while other packets can actually be considered as one block. In most PAGs with a size of less than 20 μm , one large packet is observed, which occupies more than 60% of the area of the entire PAG (Figs. 2b and 2d).

The ratio of packet sizes to block sizes is large and equals $D_{\text{packet}} \approx 12 \times D_{\text{block}}$ [8–10, 33]. This is due to the large size of the packets in PAGs with a size of 20 μm and the small thickness of the blocks. Moreover, there are usually more than three blocks in large packets, in which up to six variants of $\{111\}_\gamma \parallel (011)_\alpha$ can be observed in accordance with the Kurdjumov–Sachs orientation relationship. The high density of dislocations is observed in the studied steel (Table 3), which is 1.5 times higher than that in the steel with a similar chemical composition with 0.25 wt % C [9, 10] after similar treatment.

Table 3. Microstructure parameters of the studied steel after quenching and tempering

Steel	PAG size, μm	Packet size, μm	Block width, μm	Lath width, nm	ρ , 10^{14} m^{-2}	Volume fraction of $\gamma\text{-Fe}$, %	Size of Nb(C,N) particles, nm	Size of η -carbide (l/w), nm	Size of Fe_3C , nm
Quenching	23 ± 5	6.2 ± 1.5	0.53 ± 0.08	209 ± 33	9.4	0.86 ± 0.18	27	40/5	—
Tempering 200°C	26 ± 4	8.5 ± 1.9	0.49 ± 0.08	216 ± 34	9.1	0.63 ± 0.17	33	73/6	—
Tempering 280°C	27 ± 6	9.3 ± 2.1	0.65 ± 0.09	234 ± 29	9.3	0.54 ± 0.20	34	120/7	—
Tempering 400°C	26 ± 6	8.6 ± 1.7	0.63 ± 0.07	231 ± 35	8.4	0.45 ± 0.11	34	132/7	—
Tempering 500°C	23 ± 3	6.5 ± 1.2	0.52 ± 0.08	235 ± 33	8.6	0.21 ± 0.18	48	—	26

Residual austenite is located predominantly along high angle boundaries (HABs) of blocks of the martensitic structure. The tempering process does not lead to complete transformation of retained austenite, while its volume fraction decreases with an increase in the temperature (Table 3). This is due to the fact that retained austenite has a film morphology, while high hydrostatic stresses ensure its stability [34] up to high tempering temperatures.

Distribution of Carbides

In the quenched state, NbC carbide particles were found inside the laths (Fig. 3a). These carbides have a spherical shape, and their small size (Table 3) suggests that they are precipitated on dislocations during the quenching process [20, 35]. The martensitic matrix also contains a small amount of plate shaped particles of transition η -carbide Fe_2C with a high aspect ratio

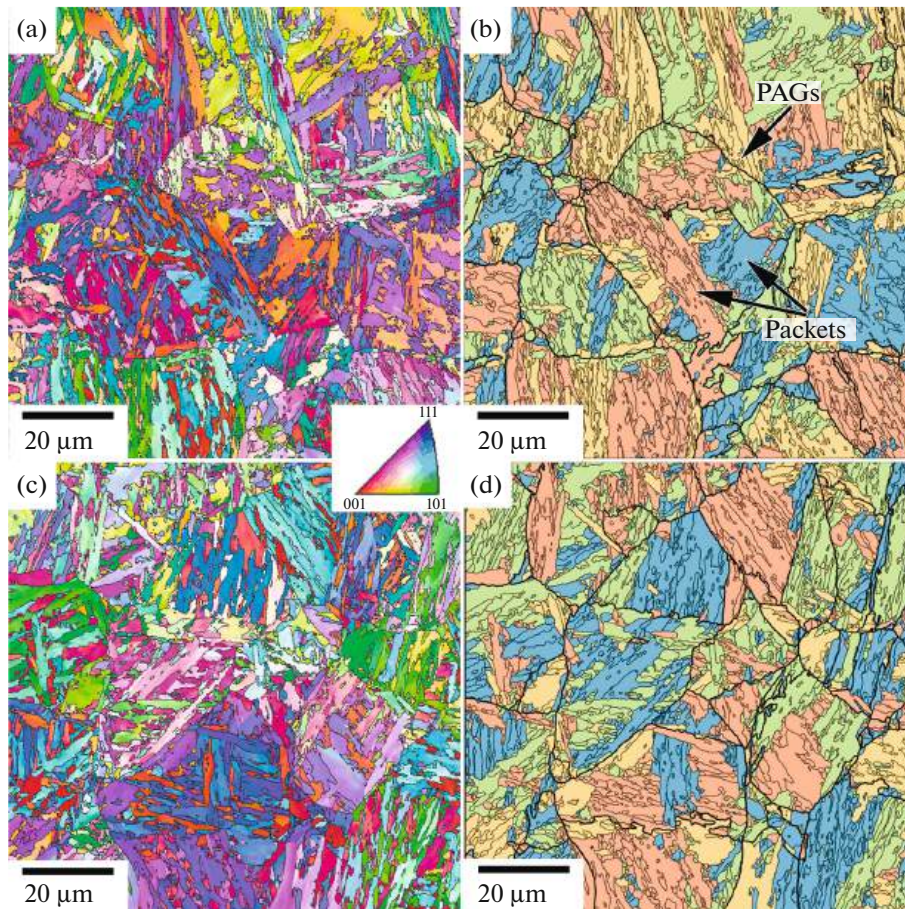


Fig. 2. Electron backscatter diffraction microphotographs of the studied steel after (a, b) quenching and (c, d) tempering at a temperature of 500°C: (a, c) misorientation maps; (b, d) maps showing different block packets in the martensitic structure. Thick black lines in figure parts (b) and (d) show the PAG boundaries, and thin lines show the block boundaries.

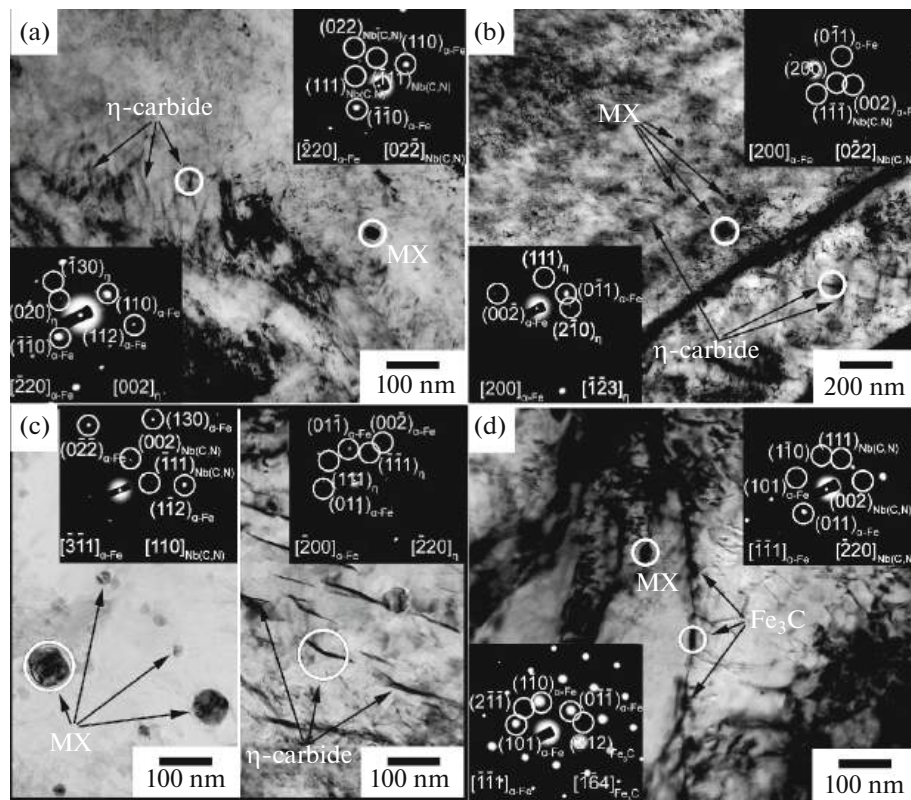


Fig. 3. Particles of the second phases in the steel structure after (a) quenching and (b–d) tempering at temperatures of (b) 200, (c) 400, and (d) 500°C. Circles in the images indicate the regions from which the corresponding electron diffraction patterns were obtained.

(l/w) of about 8 (Table 3). The thickness of these particles suggests that they are precipitated in martensite during self-tempering [10, 35].

The decomposition of martensite at tempering temperatures of $\leq 400^\circ\text{C}$ leads to the growth of NbC and η - Fe_2C carbide particles (Table 3). This indicates the precipitation of carbide NbC and η -carbide during tempering. The lamellar shape of η -carbide particles suggests the presence of a semicoherent boundary between them and the martensitic matrix [18, 23, 25, 27]. An increase in the size of η -carbide particles with an increase in the tempering temperature to 400°C is accompanied by an increase in the aspect ratio to about 19 (see Table 3 and Fig. 3c). The growth of transition carbides occurs through the migration of an incoherent transverse interface [18, 25]. The location of η -carbide plates inside martensite laths indicates a homogeneous mechanism of their nucleation [10, 18, 25].

The formation of Fe_3C cementite particles occurs with an increase in the tempering temperature to 500°C (Fig. 3d). The transition η -carbide particles dissolve. In contrast to uniformly distributed η -carbide particles, the observed cementite particles are predominantly located along the boundaries of laths and blocks. After tempering at 500°C , the maximum size of NbC carbide particles was about 90 nm, and

their minimum size was about 10 nm. The size and chemical composition of NbC carbide particles changes regardless of carbide transformations (Figs. 4 and 5).

According to Thermo-Calc calculations, MC carbides contain a substantial amount of Cr until reaching a tempering temperature of 280°C (Fig. 4a). With a further increase in the temperature, Cr is substituted by Nb and Ti. However, a study of carbon replicas revealed that MC carbonitrides mainly contain Nb and Ti with a Nb/Ti ratio of about 1.5 until reaching a temperature of 280°C , while the Cr content in these particles is less than 10 at % (Fig. 4b). With an increase in the tempering temperature from 200 to 500°C , the Nb/Ti ratio in carbonitrides MC decreases from 1.5 to 1.0 (Fig. 4b).

At tempering temperatures of $\leq 400^\circ\text{C}$, the calculated equilibrium chemical composition of cementite is dominated by Fe (Fig. 4c). At 500°C , the content of Mn and Cr in the cementite phase increases (Fig. 4c). Moreover, the $\text{Fe}/\Sigma(\text{Cr} + \text{Mn})$ ratio is 3.3. Only transition carbide particles were found in the steel structure at tempering temperatures of $\leq 400^\circ\text{C}$, which indicates that the precipitation of more stable Fe_3C with the Si content close to 0 is impossible at this tempering temperature [9]. The thermodynamically equilibrium

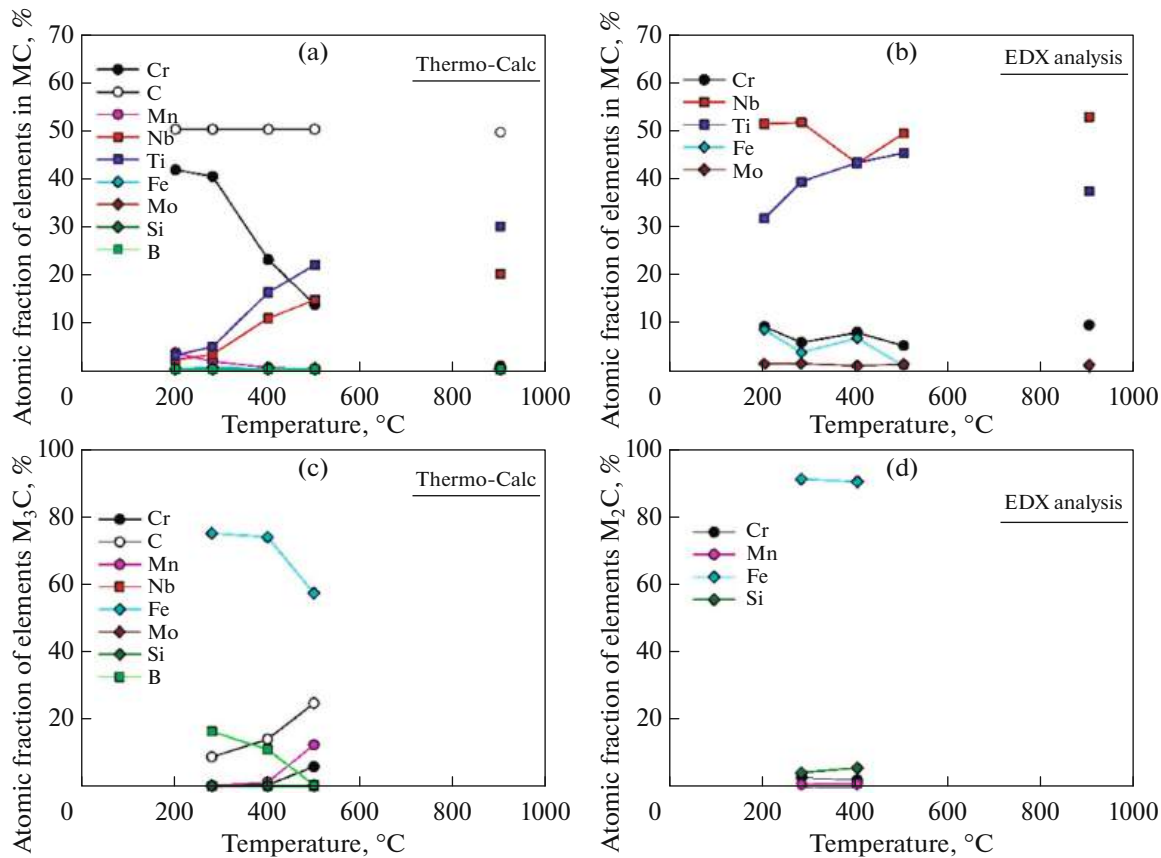


Fig. 4. Chemical compositions of (a, b) MC and (c, d) M₃C/M₂C carbide particles according to (a, c) calculations in the Thermo-Calc software package and (b, d) experimentally determined from the results of analyses of carbon replicas. In figure parts (b) and (d), the fractions of atoms of given metal elements with respect to the sum of the atoms of all carbide-forming metal elements in steel are given.

chemical composition of cementite particles at tempering temperatures of 280–400°C correlates well with the experimentally determined composition of η -carbide particles, with the exception of the Si content. This indicates that the formation of cementite particles with a more equilibrium composition is possible only under the condition of diffusion outflow of Si from the nucleating particles of this phase. That is, only transition η -carbide can be precipitated during low temperature tempering, since its formation does not require redistribution of Si. The formation of cementite in a steel containing 1.77 wt % Si can not be achieved under conditions of low temperature tempering [9].

The technique used for the preparation of carbon replicas from the etched surface of steel samples did not allow us to extract cementite particles after tempering at 500°C. Therefore, only the chemical composition of η -carbide particles is shown in Fig. 4d. The elemental analysis of η -carbide particles on extraction replicas (Fig. 4d) showed that the content of metal elements in these particles approximately corresponds to the chemical composition of the studied steel. Hence, transition carbide can be formed without considerable redistribution of substitution elements in the marten-

sitic matrix, which facilitates its precipitation during low temperature tempering. It is possible that carbon clusters in the martensitic matrix serve as nucleation sites for η -carbide [28]. At the same time, the formation of particles of other carbides, such as M₂₃C₆, M₇C₃, and M₆C, was not detected at the studied tempering temperatures.

A schematic representation of the evolution of carbide particles with an increase in the tempering temperature is shown in Fig. 5. After quenching, small NbC particles are present in the martensitic matrix, and lamellar η -Fe₂C particles are located in separate blocks (Fig. 5a). The low temperature tempering leads to the precipitation of transition η -Fe₂C carbide particles throughout the entire volume of steel and to the increases of their length and aspect ratio. The partial decomposition of martensite has no effect on the structural characteristics of this phase (see Fig. 5b and Table 3). All carbide particles formed during low temperature tempering are located inside martensite laths (Fig. 5b). The tempering at 500°C leads to complete decomposition of martensite through the precipitation of cementite along the boundaries of laths and blocks.

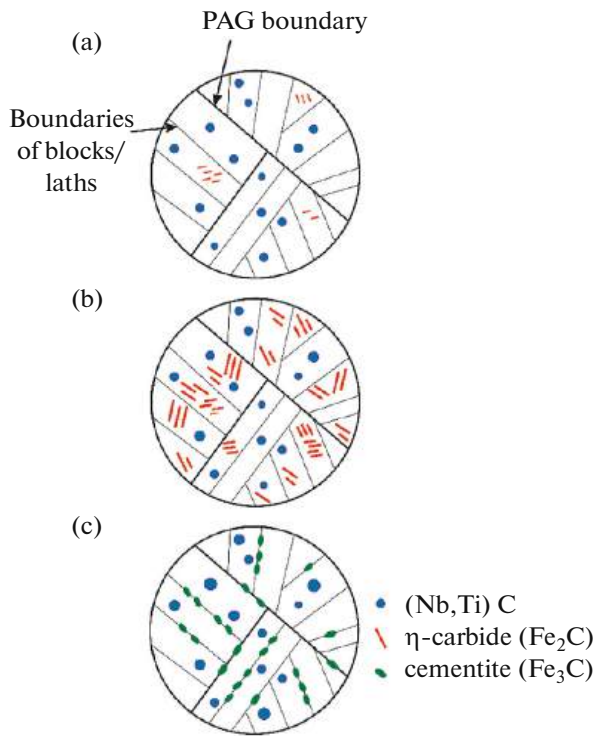


Fig. 5. Schematic representation of carbides in the studied steel subjected to (a) quenching and (b, c) tempering at temperatures of (b) 200–400 and (c) 500°C.

According to the Thermo-Calc calculation data, ferrite in a thermodynamic equilibrium with carbides contains about 0.0004 wt % C. Only NbC carbide particles remain inside the martensite laths. The tempered troostite structure is formed [36, 37].

Thus, the fundamental difference between steels with a Si content of less than 0.5 wt % and more than 1.5 wt % is the presence of clearly temperature regions of existence of transition carbides and cementite in the former. That is, the low temperature tempering and medium temperature tempering processes in this steel differ from each other mainly in the precipitated carbides, while the structural characteristics differ slightly (Table 3).

Mechanical Properties

The σ – ε engineering curves obtained under tension are shown in Fig. 6a. At tempering temperatures of $\leq 280^\circ\text{C}$, the intense strain hardening immediately follows the onset of plastic flow and the ultimate tensile strength is achieved at strain rates of $< 5\%$. At $T_{\text{temp}} \leq 400^\circ\text{C}$, an increase in the tempering temperature leads to a decrease in the degree of deformation at which the ultimate tensile strength is achieved. This effect of tempering temperature is usually correlated with an increase in the specific volume of dispersed particles located in the martensitic matrix. At a tem-

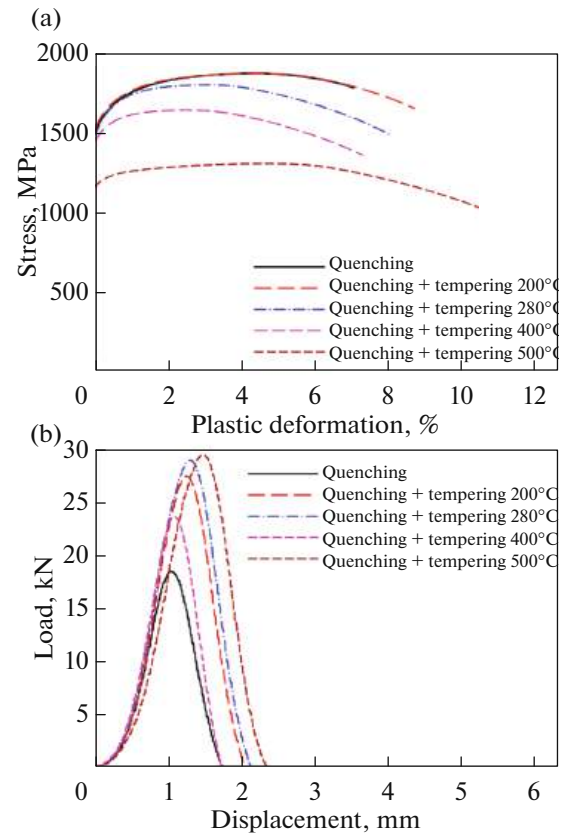


Fig. 6. (a) Deformation curves and (b) the dependences of the load on the move of the pendulum, which are obtained during impact tests of the steel after the Q&T processing.

pering temperature of 500°C , the stage of strain hardening becomes longer, the magnitude of strain hardening decreases, and the onset of neck formation shifts toward higher degrees of deformation. This type of σ – ε curves is typical of the deformation accompanied by the movement of dislocations along martensitic laths [36, 38] when dispersion strengthening is provided by chains of carbides located along the boundaries of laths and blocks.

At $T_{\text{temp}} \leq 280^\circ\text{C}$, the (value of) yield strength increases because of increasing the contribution of dispersion strengthening. It should be noted that the steel is in a highly plastic state after quenching (Table 4), which confirms the redistribution of carbon from the martensitic matrix into the Cottrell atmospheres during cooling in the quenching process [8, 33]. An increase in the tempering temperature above 280°C leads to a decrease in both the yield strength and ultimate strength values (Table 4). This is associated with an increase in the degree of martensite decomposition and the enlargement of transition η -carbide particles at 400°C and with the complete decomposition of martensite and the replacement of η -carbides with grain boundary chains of cementite at 500°C . The difference between the ultimate tensile and yield strength

Table 4. Mechanical properties of the studied steel after the Q&T processing

Q&T	Yield strength, MPa	Ultimate tensile strength, MPa	Total elongation, %
Quenching	1280	1870	7.5
Tempering 200°C	1430	1870	9.0
Tempering 280°C	1490	1800	8.0
Tempering 400°C	1420	1640	7.5
Tempering 500°C	1160	1300	10.5

Table 5. Mechanical characteristics and proportions of various zones on the fracture surface of the steel samples after impact tests performed at room temperature after quenching and tempering

Q&T	Impact toughness, J/cm ²	P_M , kN	Proportion of the lateral zone of ductile fracture, %	Proportion of the fracture-inhibition zone of crack propagation, %
Quenching	17	18	3.6	1.0
Tempering 200°C	31	28	8.6	1.7
Tempering 280°C	35	29	13.8	4.7
Tempering 400°C	22	23	5.6	1.8
Tempering 500°C	37	29	14.2	5.7

values decreased by 70% from 440 to 140 MPa when the tempering temperature increased from 200 to 500°C, which indicates that transition carbide particles located in the matrix contribute to the accumulation of dislocations during tension to a greater extent than grain boundary carbide particles. With an increase in the tempering temperature above 280°C, the relative elongation increases by 30% (Table 4). These data indicate that the studied steel can be certified as a high strength steel with transition carbides. It is superior in strength and ductility to steel AISI4340 and is slightly inferior to aviation steel 300M, which is the main high strength steel (Table 1). Tempering leads to an almost twofold increase in the impact toughness of the studied steel (Table 5). It should be noted that the impact toughness of the Fe–0.34C steel after tempering is higher than that of steels AISI4340 and 300M (Table 1). The resulting microstructure of the studied steel with a low carbon content made it possible to achieve high impact toughness combined with high strength parameters despite the absence of Ni.

Irreversible tempering-induced brittleness, which manifests itself in the Fe–0.34C steel after tempering at a temperature of 400°C, is usually associated either with the formation of cementite films at the retained austenite/martensite interfaces or with the formation of elongated cementite along the boundaries of laths and blocks [6, 8]. The formation of cementite was not detected at tempering temperatures of $\leq 400^\circ\text{C}$ in the studied steel, in contrast to steel AISI4340, in which a large amount of cementite is observed after tempering at 350°C [39]. Irreversible tempering-related brittleness in high strength low alloyed steels with transition carbides may be caused by an increase in the effective

grain size for brittle fracture. The effective grain size is taken to be the distance between the boundaries, within which the crack does not substantially change its direction. An increase in this size is associated with the decomposition of retained austenite located along the boundaries of blocks and/or the disappearance of carbon segregations along the HABs [8]. As a result, block boundaries cease to serve as an obstacle to the propagation of chips. In addition, the coarsening of transition η -carbide particles reduces impact toughness [8]. Suppression of the precipitation of cementite along the boundaries due to the introduction of 1.77 wt % of Si into steel reduces the extent of decreasing the impact toughness in the temperature range of irreversible tempering-related embrittlement [8]. The tempering of the Fe–0.34C steel at a temperature of 500°C allows one to increase the impact toughness by almost 65% when compared to tempering at 400°C and by a factor of almost 2 relative to the impact toughness after quenching (Table 5), despite the formation of cementite chains along the boundaries of laths, blocks, packets, and PAGs, which is considered the cause of tempering-induced brittleness in steels of the AISI4340 type [6, 8, 39]. Accordingly, the formation of grain boundary cementite particles in the studied steel not only does not lead to its embrittlement, but also provides high impact toughness and plasticity values (see Fig. 5 and Tables 4 and 5).

Figure 6b shows the dependence of the load on the displacement of the pendulum during impact tests. One can see that the type of curves is the same for all processing modes. In all load–displacement curves, only the point of maximum load (P_M) is observed among the four points characterizing the behavior of

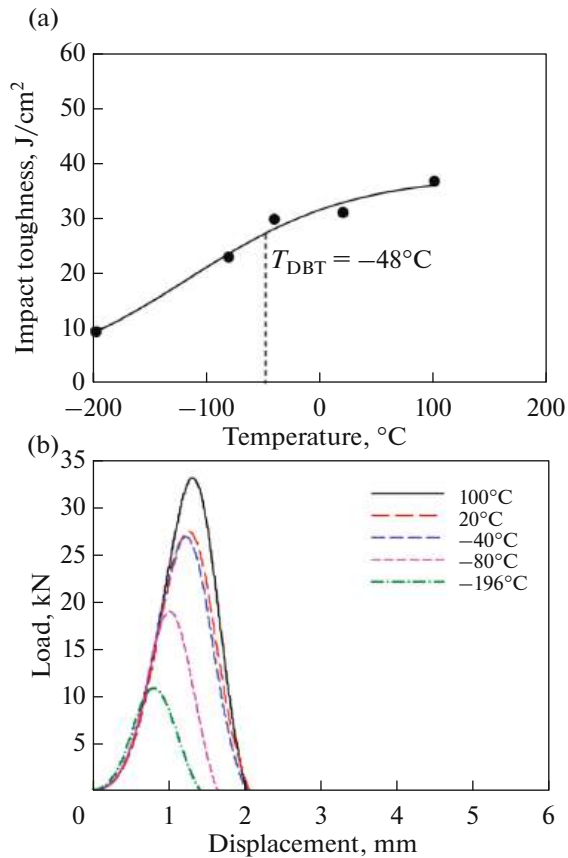


Fig. 7. (a) Effect of the test temperature on the impact toughness and (b) the dependence of the load on the deflection (displacement) value for the steel after tempering at a temperature of 200°C.

the material during these tests [40, 41]. After reaching the maximum load, the crack propagation stage immediately begins. The increase in the energy spent to initiate a crack of a critical size and the energy spent for its propagation is accompanied by an increase in the P_M value and leads to an increase in the impact toughness. Low temperature tempering at 200 and 280°C increases the P_M value when compared to quenching. A similar maximum load value is observed after tempering at 500°C, while the P_M value achieved after tempering at 400°C is smaller (Table 5). Thus,

the precipitation of both transition carbides at a tempering temperature of up to 280°C and cementite chains along the boundaries of laths and blocks provides a relatively high critical length of a crack that is capable of propagation.

It should be noted that it is difficult to understand the nature of destruction from the results of dynamic mechanical tests, since the curves do not contain the P_F point, which is associated with the transition from stable to unstable crack propagation. In addition, the slope of the load–displacement curve to the right of the P_M point indicates that a significant amount of energy is spent on crack propagation, which is not typical of unstable crack propagation [40, 41]. Given that the displacement of the pendulum is much less than the thickness of the sample, accelerated crack propagation occurs.

The ductile–brittle transition (DBT) was studied on steel samples tempered at a temperature of 200°C (Fig. 7). The weak influence of the test temperature in the range of $T \geq -80^\circ\text{C}$ on the impact toughness is a feature of the steel with transition carbides (Table 6).

An increase in the test temperature from -80°C to 100°C leads to an increase in the impact toughness by 56% (Table 6), which is associated with an increase in the P_M value (Fig. 7b). Moreover, the impact toughness of the steel at a test temperature of -80°C does not fall below 20 J/cm^2 (Table 6). This value is considered sufficient to stop the propagation of a crack under dynamic loading and approximately corresponds to the conventional boundary of the transition from ductile to brittle fracture [41]. That is, the impact toughness of the studied high strength steel with transition carbides is hardly sensitive to operating temperatures.

The DBT temperature defined as the temperature corresponding to 50% of the difference between the maximum and minimum impact toughness values was about -50°C (Fig. 7a). With a decrease in the test temperature to -196°C , embrittlement occurs because of decreasing the P_M value by a factor of almost 3 with respect to the P_M value achieved during the test run at 100°C . It should be noted that the obtained impact toughness values are generally typical of high strength steels with transition carbides and low tempered martensite [7, 42].

Table 6. Mechanical characteristics and proportions of various zones on the fracture surface of samples tempered at 200°C and subjected to impact tests

Parameters	Temperature				
	100°C	20°C	-40°C	-80°C	-196°C
Impact toughness, J/cm^2	36	31	29	23	9
P_M , kN	33	28	27	19	11
Proportion of the lateral zone of ductile fracture, %	19.6	8.6	11.9	4.2	0.3
Proportion of the fracture-inhibition zone of crack propagation, %	11.9	1.7	2.1	1.0	0.8

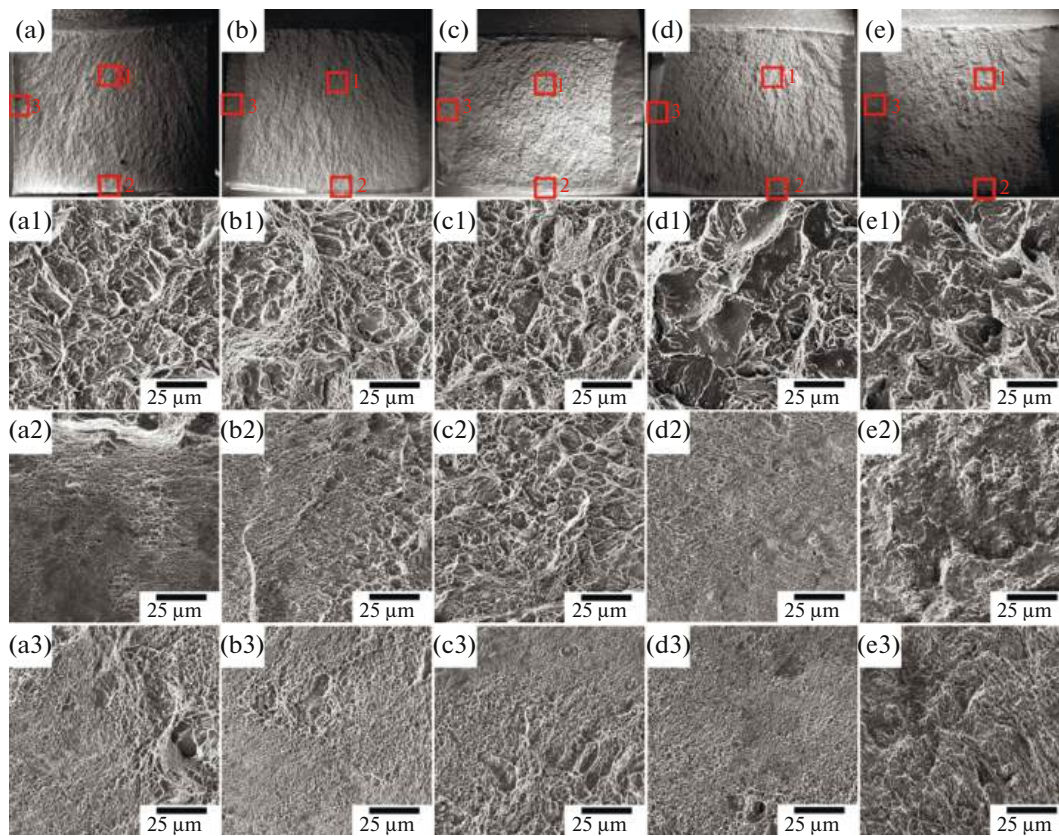


Fig. 8. SEM images of the fracture surface of samples after impact tests performed at room temperature after (a) quenching and (b–e) tempering at temperatures of (b) 200, (c) 280, (d) 400, and (e) 500°C. Figure parts (a1–e1) correspond to crack propagation zones, parts (a2–e2) correspond to the rupture zones, and parts (a3–e3) correspond to zones of destruction by a shear mechanism.

Figure 8 shows the fracture surface images of the studied steel samples after impact toughness tests performed at room temperature.

Three fracture regions can be distinguished in Figs. 8a–8e. These are central zone 1 in which a crack mainly propagates by the quasi-cleavage mechanism characteristic of steels with a packet martensite structure [6, 8–11, 41] (corresponds to parts a1, b1, c1, d1, and e1 in Fig. 8), fracture zone 2 with inhibited propagation of the main crack [20, 22, 40, 41] (corresponds to parts a2, b2, c2, d2, and e2 in Fig. 8), and lateral zone 3 of ductile fracture characteristic of low alloyed steels with a strength above 1200 MPa [20, 22] (corresponds to parts a3, b3, c3, d3, and e3 in Fig. 8). After hardening, the areas of zones 2 and 3 are reduced. Accordingly, the contribution of ductile fracture to impact toughness is insignificant. Small dimples are observed only on some detachment ridges (Fig. 8a1). Impact toughness is determined by the mechanism of quasi-cleavage fracture during crack propagation (see Table 5 and Fig. 8a). The cleavage occurring typically within blocks and, in rare cases, in the whole packet is a feature of the mechanism of propagation of the main crack (Fig. 8a1). Low temperature tempering leads to

an increase in the proportion of ductile fracture both due to increases in the areas of zones 2 and 3 (Table 5) and due to an increase in the proportion of ductile fracture in zone 1 (Figs. 8b and 8c). Tempering at 400°C reduces the proportion of ductile fracture (see Table 5 and Fig. 8d). This change may be associated with an increase in the effective grain size during brittle fracture due to increases in the particle size and in the volume fraction of transition carbides [8, 43, 44].

Tempering at 500°C increases the proportion of ductile fracture both due to increases in the areas of zones 2 and 3, and due to the appearance of tear-associated dimples on the ridges around most of the packets (Fig. 8e). Simultaneously, cleavage occurs within individual packets predominates (Fig. 8e1). Crack propagation in the steel undergone tempering at 400 and 500°C occurs along individual boundaries of packets and PAGs and does not completely cover these structural elements of martensite (Figs. 8d1 and 8e1).

Impact tests of steel samples after tempering at 200°C showed that a decrease in the impact toughness with decreasing test temperature is associated with a decrease in the proportion of ductile fracture both due

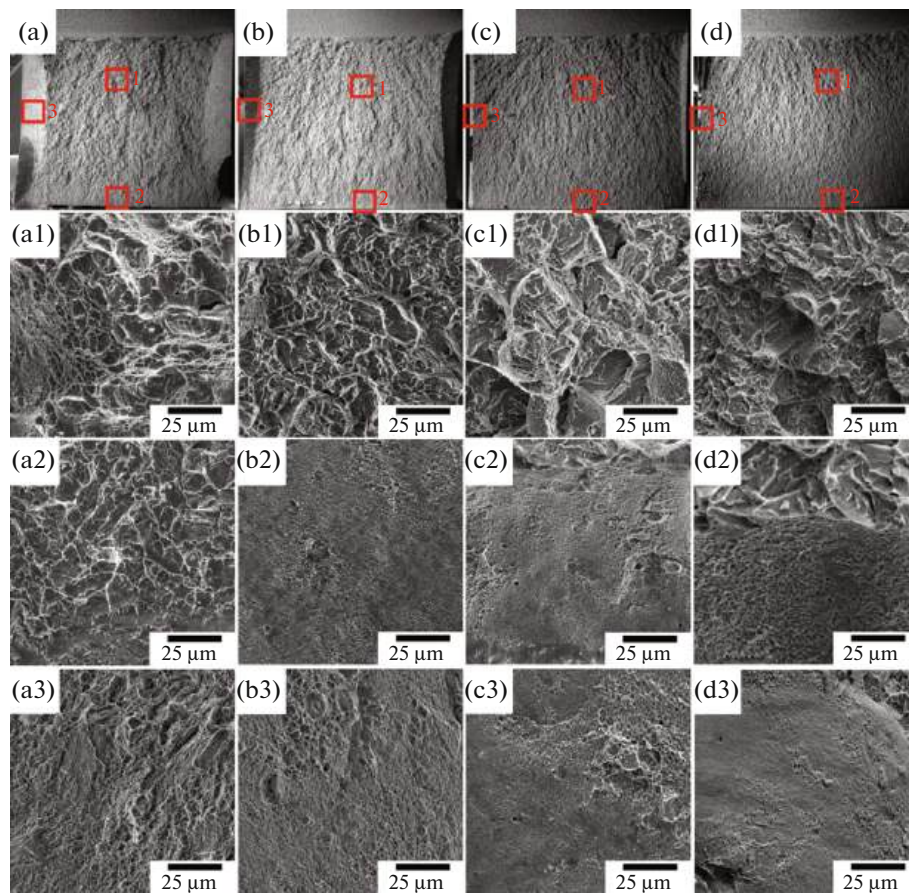


Fig. 9. SEM images of the fracture surface of samples of the studied steel tempered at a temperature of 200°C after impact tests performed at temperatures of (a) 100, (b) -40, (c) -80, and (d) -196°C. Figure parts (a1–d1) correspond to crack propagation zones, parts (a2–d2) correspond to the rupture zones, and parts (a3–d3) correspond to zones of destruction by a shear mechanism.

to decreases in the areas of zones 2 and 3 (see Table 6 and Fig. 9) and due to a decrease in the area of ductile fracture in zone 1 (Figs. 9a1–c1).

At -80°C, intergranular brittle fracture is detected around individual packets and PAGs, as well as quasi-cleavage within some packets (Fig. 9c1). At -196°C, no ductile fracture was observed in the zone of critical crack propagation even on the ridges of separation (Fig. 9d1), and the areas of zones 2 and 3 were negligibly small.

CONCLUSIONS

The mechanical properties, microstructure, and distribution of carbide particles in the Fe-0.34C medium carbon steel after Q&T are studied. The following conclusions are drawn.

(1) After austenitization at 900°C and quenching, lath martensite inherits the boundaries of the prior austenite grain with a size of 23 μm and includes packets, blocks, and laths. The size of the packets and the width of the blocks and laths in this state are 6.2 and 0.53 μm, and 209 nm, respectively. The dislocation

number density calculated by analyzing the EBSD patterns is high and equals $9.4 \times 10^{14} \text{ m}^{-2}$. There are Nb(C,N) carbide particles and a small amount of transition η-carbide particles precipitated during self-tempering inside the laths.

(2) During low-temperature tempering (up to 400°C), transition η-carbide particles are precipitated. Their average size and specific volume increase with an increase in the tempering temperature. Medium temperature tempering at a temperature of 500°C leads to the formation of cementite particles in the form of chains along the lath and block boundaries. This process is accompanied by complete dissolution of transition η-carbides.

(3) The increase of the yield strength from 1230 MPa in the quenched state to 1490 MPa after tempering at 280°C is associated with the precipitation of η-carbide particles. A total elongation of about 8% and a ultimate tensile strength of about 1800 MPa hardly depend on the low temperature tempering temperature. The tempering at 400°C leads to a decrease in the strength and ductility. After tempering at 500°C, the yield strength decreases to 1160 MPa, and the ulti-

mate tensile strength decreases to 1300 MPa with an increase in the elongation to about 10%.

(4) The impact toughness increases from 17 J/cm² after quenching to 37 J/cm² after tempering at 280°C. An increasing in the tempering temperature from 280 to 400°C leads to a decrease in the impact toughness from 37 to 22 J/cm². The complete decomposition of martensite at 500°C increases the impact toughness.

(5) The DBT temperature of the studied steel after tempering at 200°C is about –50°C. The decrease of the impact toughness in the range of test temperatures from –80 to –196°C is associated with a decrease in the proportion of ductile fracture and the development of intergranular brittle fracture. In the temperature range from –80 to +100°C, the material has acceptable impact toughness. The weak temperature dependence of the impact toughness was observed.

(6) The studied Fe–0.34C steel can be certified as a high strength steel with transition carbides. It is superior in strength, ductility, and toughness to steel AISI4340 and nearly corresponds to that of the steel 300M considered the main high strength aviation steel.

FUNDING

This study was supported by the Megagrant program from the Ministry of Science and Higher Education of the Russian Federation (State agreement no. 075-15-2021-572).

CONFLICT OF INTEREST

The authors of this work declare that they have no conflicts of interest.

REFERENCES

- V. V. Ryabov, E. I. Khlusova, S. A. Golosienko, and G. D. Motovilina, “New steels for agricultural machine building,” *Metallurgist* **59**, 505–513 (2015).
<https://doi.org/10.1007/s11015-015-0132-3>
- N. Fonstein, *Advanced High Strength Sheet Steels: Physical Metallurgy, Design, Processing, and Properties* (Springer, Cham, 2015).
<https://doi.org/10.1007/978-3-319-19165-2>
- J. Zhao and Z. Jiang, “Thermomechanical processing of advanced high strength steels,” *Prog. Mater. Sci.* **94**, 174–242 (2018).
<https://doi.org/10.1016/j.pmatsci.2018.01.006>
- G. Malakondaiah, M. Srinivas, and P. R. Rao, “Ultra-high-strength low-alloy steels with enhanced fracture toughness,” *Prog. Mater. Sci.* **42**, 209–242 (1997).
[https://doi.org/10.1016/s0079-6425\(97\)00016-9](https://doi.org/10.1016/s0079-6425(97)00016-9)
- J. Li, D. Zhan, Z. Jiang, H. Zhang, Yo. Yang, and Ya. Zhang, “Progress on improving strength–toughness of ultra-high strength martensitic steels for aerospace applications: A review,” *J. Mater. Res. Technol.* **23**, 172–190 (2023).
<https://doi.org/10.1016/j.jmrt.2022.12.177>
- G. Krauss, “Steels,” in *Processing Structure, and Performance* (ASM Int., Metals Park, Ohio, 2005), pp. 230–232.
<https://doi.org/10.31399/asm.tb.spsp2.9781627082655>
- Y. Tomita, “Development of fracture toughness of ultrahigh strength, medium carbon, low alloy steels for aerospace applications,” *Int. Mater. Rev.* **45**, 27–37 (2000).
<https://doi.org/10.1179/095066000771048791>
- R. Mishnev, Yu. Borisova, T. Kniazuk, S. Gaidar, and R. Kaibyshev, “Quench and tempered embrittlement of ultra-high-strength steels with transition carbides,” *Metals* **13**, 1399 (2023).
<https://doi.org/10.3390/met13081399>
- S. Borisov, Yu. Borisova, E. Tkachev, T. Kniazuk, and R. Kaibyshev, “Tempering behavior of a Si-rich low-alloy medium-carbon steel,” *Metals* **13**, 1403 (2023).
<https://doi.org/10.3390/met13081403>
- E. Tkachev, S. Borisov, A. Belyakov, T. Kniazuk, O. Vagina, S. Gaidar, and R. Kaibyshev, “Effect of quenching and tempering on structure and mechanical properties of a low-alloy 0.25C steel,” *Mater. Sci. Eng., A* **868**, 144757 (2023).
<https://doi.org/10.1016/j.msea.2023.144757>
- V. Dudko, D. Yuzbekova, S. Gaidar, S. Vetrova, and R. Kaibyshev, “Tempering behavior of novel low-alloy high-strength steel,” *Metals* **12**, 2177 (2022).
<https://doi.org/10.3390/met12122177>
- V. K. Euser, D. L. Williamson, K. O. Findley, A. J. Clarke, and J. G. Speer, “The role of retained austenite in tempered martensite embrittlement of 4340 and 300-M steels investigated through rapid tempering,” *Metals* **11**, 1349 (2021).
<https://doi.org/10.3390/met11091349>
- V. M. Schastlivtsev, Yu. V. Kaletina, E. A. Fokina, and A. Yu. Kaletin, “On the role of retained austenite in the structure of alloyed steels and the effect of external factors,” *Phys. Met. Metallogr.* **115**, 904–917 (2014).
<https://doi.org/10.1134/s0031918x14090105>
- L. Liu, B. R. Shan, Z. H. Zhang, T. T. Li, S. Z. Zhao, C. N. Jing, T. Lin, and J. R. Zhao, “Effect of cyclic quenching on the austenite stability and work hardening behavior of medium-Mn quenching and partitioning steel enabled by intercritical annealing,” *Phys. Met. Metallogr.* **123**, 1451–1460 (2022).
<https://doi.org/10.1134/s0031918x2110104x>
- J. G. Speer, “Phase transformations in quenched and partitioned steels,” in *Phase Transformations in Steels: Diffusionless Transformations, High Strength Steels, Modelling and Advanced Analytical Techniques*, Ed. by E. Pereloma and D. V. Edmonds, Woodhead Publishing Series in Metals and Surface Engineering, Vol. 2 (Elsevier, Cambridge, 2012), pp. 247–270.
<https://doi.org/10.1533/9780857096111.2.247>
- E. Kozeschnik and H. K. D. H. Bhadeshia, “Influence of silicon on cementite precipitation in steels,” *Mater. Sci. Technol.* **24**, 343–347 (2008).
<https://doi.org/10.1179/174328408x275973>
- H. K. D. H. Bhadeshia, D. E. Laughlin, and K. Hono, “Physical metallurgy of steels,” in *Physical Metallurgy*, Ed. by D. E. Laughlin and K. Hono (Elsevier, Amsterdam, 2014), pp. 2157–2214.
<https://doi.org/10.1016/b978-0-444-53770-6.00021-6>
- D. A. Porter, K. E. Easterling, and M. Y. Sherif, *Phase Transformations in Metals and Alloys* (CRC Press, Boca Raton, Fla., 2009).
<https://doi.org/10.1201/9781003011804>

19. M. V. Maisuradze, Yu. V. Yudin, A. A. Kuklina, and D. I. Lebedev, "Formation of microstructure and properties during isothermal treatment of aircraft building steel," *Metallurgist* **65**, 1008–1019 (2022). <https://doi.org/10.1007/s11015-022-01241-1>
20. S. Vervynckt, K. Verbeken, B. Lopez, and J. J. Jonas, "Modern HSLA steels and role of non-recrystallisation temperature," *Int. Mater. Rev.* **57**, 187–207 (2012). <https://doi.org/10.1179/1743280411y.0000000013>
21. D. P. Field, "Recent advances in the application of orientation imaging," *Ultramicroscopy* **67**, 1–9 (1997). [https://doi.org/10.1016/s0304-3991\(96\)00104-0](https://doi.org/10.1016/s0304-3991(96)00104-0)
22. F. Niessen, T. Nyyssönen, A. A. Gazder, and R. Hielscher, "Parent grain reconstruction from partially or fully transformed microstructures in *MTEX*," *J. Appl. Crystallogr.* **55**, 180–194 (2022). <https://doi.org/10.1107/s1600576721011560>
23. M. Calcagnotto, D. Ponge, E. Demir, and D. Raabe, "Orientation gradients and geometrically necessary dislocations in ultrafine grained dual-phase steels studied by 2D and 3D EBSD," *Mater. Sci. Eng., A* **527**, 2738–2746 (2010). <https://doi.org/10.1016/j.msea.2010.01.004>
24. R. Mishnev, Yu. Borisova, S. Gaidar, T. Kniazniuk, O. Vagina, and R. Kaibyshev, "Q&P response of a medium carbon low alloy steel," *Metals* **13**, 689 (2023). <https://doi.org/10.3390/met13040689>
25. T. Wang, J. Du, and F. Liu, "Modeling competitive precipitations among iron carbides during low-temperature tempering of martensitic carbon steel," *Materialia* **12**, 100800 (2020). <https://doi.org/10.1016/j.mtla.2020.100800>
26. D. T. Pierce, D. R. Coughlin, D. L. Williamson, K. D. Clarke, A. J. Clarke, J. G. Speer, and E. De Moor, "Characterization of transition carbides in quench and partitioned steel microstructures by Mössbauer spectroscopy and complementary techniques," *Acta Mater.* **90**, 417–430 (2015). <https://doi.org/10.1016/j.actamat.2015.01.024>
27. W. Lu, M. Herbig, C. H. Liebscher, L. Morsdorf, R. K. W. Marceau, G. Dehm, and D. Raabe, "Formation of eta carbide in ferrous martensite by room temperature aging," *Acta Mater.* **158**, 297–312 (2018). <https://doi.org/10.1016/j.actamat.2018.07.071>
28. Z. Xiong, I. Timokhina, and E. Pereloma, "Clustering, nano-scale precipitation and strengthening of steels," *Prog. Mater. Sci.* **118**, 100764 (2021). <https://doi.org/10.1016/j.pmatsci.2020.100764>
29. R. M. Horn and R. O. Ritchie, "Mechanisms of tempered martensite embrittlement in low alloy steels," *Metall. Trans. A* **9**, 1039–1053 (1978). <https://doi.org/10.1007/bf02652208>
30. H. Kitahara, R. Ueji, N. Tsuji, and Yo. Minamino, "Crystallographic features of lath martensite in low-carbon steel," *Acta Mater.* **54**, 1279–1288 (2006). <https://doi.org/10.1016/j.actamat.2005.11.001>
31. G. Miyamoto, N. Iwata, N. Takayama, and T. Furuhashi, "Mapping the parent austenite orientation reconstructed from the orientation of martensite by EBSD and its application to ausformed martensite," *Acta Mater.* **58**, 6393–6403 (2010). <https://doi.org/10.1016/j.actamat.2010.08.001>
32. V. M. Gundyrev, V. I. Zeldovich, and V. M. Schastlivtsev, "Crystallographic analysis and mechanism of martensitic transformation in Fe alloys," *Phys. Met. Metallogr.* **121**, 1045–1063 (2020). <https://doi.org/10.1134/s0031918x20110046>
33. E. I. Galindo-Nava and P. E. J. Rivera-Díaz-Del-Castillo, "A model for the microstructure behaviour and strength evolution in lath martensite," *Acta Mater.* **98**, 81–93 (2015). <https://doi.org/10.1016/j.actamat.2015.07.018>
34. N. Nakada, Yu. Ishibashi, T. Tsuchiyama, and S. Takaki, "Self-stabilization of untransformed austenite by hydrostatic pressure via martensitic transformation," *Acta Mater.* **110**, 95–102 (2016). <https://doi.org/10.1016/j.actamat.2016.03.048>
35. R. A. Vorobev, V. N. Dubinskii, and V. V. Evstifeeva, "Effect of the processes of self-tempering and tempering on the mechanical characteristics and the character of fracture of low-carbon martensitic steel quenched in air," *Phys. Met. Metallogr.* **120**, 989–994 (2019). <https://doi.org/10.1134/S0031918X19100132>
36. V. Dudko, A. Belyakov, and R. Kaibyshev, "Evolution of lath substructure and internal stresses in a 9% Cr steel during creep," *ISIJ Int.* **57**, 540–549 (2017). <https://doi.org/10.2355/isijinternational.isijint-2016-334>
37. M. V. Odnobokova, A. Yu. Kipelova, A. N. Belyakov, and R. O. Kaibyshev, "Mechanical behavior and brittle–ductile transition of high-chromium martensitic steel," *Phys. Met. Metallogr.* **117**, 390–398 (2016). <https://doi.org/10.1134/s0031918x16040098>
38. J. Inoue, A. Sadeghi, and T. Koseki, "Slip band formation at free surface of lath martensite in low carbon steel," *Acta Mater.* **165**, 129–141 (2019). <https://doi.org/10.1016/j.actamat.2018.11.026>
39. C. L. Briant, "Role of carbides in tempered martensite embrittlement," *Mater. Sci. Technol.* **5**, 138–147 (1989). <https://doi.org/10.1179/mst.1989.5.2.138>
40. A. Chatterjee, A. Moitra, A. K. Bhaduri, D. Chakrabarti, and R. Mitra, "Effect of heat treatment on ductile–brittle transition behaviour of 9Cr–1Mo steel," *Procedia Eng.* **86**, 287–294 (2014). <https://doi.org/10.1016/j.proeng.2014.11.040>
41. *Mechanical Testing and Evaluation*, Ed. by H. Kuhn and D. Medlin, ASM Handbook, Vol. 8 (ASM International, 2000). <https://doi.org/10.31399/asm.hb.v08.9781627081764>
42. G. Krauss and D. K. Matlock, "Effects of strain hardening and fine structure on strength and toughness of tempered martensite in carbon steels," *J. Physique IV* **05**, C8–51 (1995). <https://doi.org/10.1051/jp4:1995806>
43. T. Hanamura, F. Yin, and K. Nagai, "Ductile–brittle transition temperature of ultrafine ferrite/cementite microstructure in a low carbon steel controlled by effective grain size," *ISIJ Int.* **44**, 610–617 (2004). <https://doi.org/10.2355/isijinternational.44.610>
44. J. W. Morris Jr., "On the ductile–brittle transition in lath martensitic steel," *ISIJ Int.* **51**, 1569–1575 (2011). <https://doi.org/10.2355/isijinternational.51.1569>

Translated by O. Kadkin

Publisher's Note. Pleiades Publishing remains neutral with regard to jurisdictional claims in published maps and institutional affiliations.